Advances in Susceptibility-Weighted Imaging (SWI) and Quantitative Susceptibility Mapping (QSM)

Josef Pfeuffer[1], Korbinian Eckstein[2], Ashley Wilton Stewart[2], Marcel Dominik Nickel[1], Jin Jin[3], Heiko Meyer[1], Steffen Bollmann[2], Kieran O'Brien[3]

[1]Application Development, Siemens Healthineers AG, Erlangen, Germany
[2]The University of Queensland, Brisbane, Australia
[3]Siemens Healthcare Pty Ltd, Brisbane, Australia

Objectives

- Demonstrate enhanced performance of susceptibility-weighted imaging (SWI) in high-susceptibility brain regions (e.g., frontal lobe, ear canals) through improved phase processing.
- Achieve signal-to-noise improvements in SWI via the utilization of multi-echo SWI acquisition and processing techniques.
- Provide a comprehensive overview of processing methodologies and algorithms applied in the generation of quantitative susceptibility mapping (QSM) and susceptibility map-weighted imaging (SMWI).
- Demonstrate the advantages gained from using 3D deep learning *k*-space-to-image reconstruction (Deep Resolve Boost).
- Enable visualization of nigrosome 1 "swallow tail" patterns in the substantia nigra using a 0.65 mm isotropic protocol, accomplished within a three-minute acquisition.

The data shown in this article uses research sequences and scanner inline reconstructions at 3 Tesla[1] with software version *syngo* MR XA60. The 3T MR scanners include MAGNETOM Vida, MAGNETOM Skyra, and MAGNETOM Prisma. Three-dimensional gradient-echo imaging (3D-GRE) and 3D echo-planar imaging (3D-EPI) sequences are used in this article.

Introduction

There has been a growing interest in image contrasts derived from phase images obtained from T2*-weighted gradient-echo (GRE) acquisitions. The fundamental principles of Susceptibility-Weighted Imaging (SWI) were comprehensively expounded by J. R. Reichenbach and E. M. Haacke [1] in 2001. SWI is now a highly valuable contrast for a wide range of clinical applications. Valuable insights into the evolution and application of SWI principles can be found in the related references [2–5]. The recently proposed treatments for Alzheimer's disease will likely increase the utilization of SWI to regularly monitor potential side effects. These "Disease-Modifying Therapies" (DMT) rely on serial MR imaging with T2*-weighted and/or SWI imaging to check for the presence of microhemorrhages and superficial siderosis known as Amyloid-Related Imaging Abnormalities of Hemorrhage (ARIA-H) [6]. The recent Wave-CAIPI SWI product, illustrated in Figure 1, could be a useful addition to this clinical application.

Another phase imaging-based technique known as Quantitative Susceptibility Mapping (QSM) [4, 7–9] can also provide additional information about the apparent magnetic susceptibility of underlying tissues. QSM can provide information about the "biometal" content in tissues, including paramagnetic iron (Fe^{2+}), contrast agents (Gd, Fe^{2+}), and diamagnetic calcium (Ca^{2+}). QSM has the potential to provide new clinical insights into a variety of diseases, allowing for enhanced understanding and diagnosis. Examples include the following:

- Inflammation and Multiple Sclerosis (MS) [4, 10–13]
- Calcification [4] versus hemorrhaging in the brain [14] and in tumors [15]
- Support for presurgical planning for Parkinson's disease [16, 17]
- Iron accumulation in normal aging and in neurodegenerative diseases [18–24]
- Iron overload in the liver [25]
- Bone mineralization [26]

QSM reconstruction involves several sophisticated processing steps which are currently relegated to offline execution instead of using streamlined inline processing on the scanner. Furthermore, even though both SWI and QSM rely on the same underlying data, the lack of compatibility

[1]*Work in progress: The research application is currently under development and is not for sale in the U.S. and in other countries. Its future availability cannot be ensured.*

between the various processing techniques in existing software pipelines has hindered the seamless dual application of SWI and QSM post-processing steps.

In this work, we will showcase results from a research implementation which explored further enhancements to clinical GRE acquisitions attainable through the incorporation of parallel imaging in both directions with CAIPIRINHA acceleration, and adopting multi-echo acquisitions with suitable echo combinations. The SWI reconstruction pipeline on the scanner was extended to enable compatibility with advanced acceleration techniques, including CAIPIRINHA. The pipeline also utilizes an additional Laplacian unwrapping pre-processing step before high-pass filtering, and supports multi-echo datasets.

Magnitude and phase images were previously exported for processing in offline QSM packages. The reconstruction pipeline of the research implementation sequence includes two research QSM methods: TGV and MEDI, as detailed below. These methods run parallel to SWI, providing SWI, QSM maps, and QSM-derived images inline.

Lastly, the benefits of more efficient 3D-EPI sequences are also showcased for both SWI and QSM. This is made possible by integrating a novel deep learning *k*-space-to-image-space reconstruction. Through the utilization of the new 3D Deep Resolve Boost and super-resolution 3D Deep Resolve Sharp features, now available on MAGNETOM scanners, the imaging capabilities for both SWI and QSM applications are further amplified.

Improved Susceptibility-Weighted Imaging (SWI)

The recently available product Wave-CAIPI SWI is an innovative SWI technique exclusive to Siemens Healthineers [27, 28]. Figure 1 compares the speed and image quality of Wave-CAIPI SWI to current standard SWI, obtained using a MAGNETOM Vida with a voxel size of 0.6 × 0.6 × 2.0 mm^3. This novel SWI approach allows for a substantial acceleration in diagnostic single-echo 3D-SWI, enabling imaging in half the acquisition time.

Multi-echo SWI data can be acquired with the research application, and it incorporates 3D Laplacian phase unwrapping for improved phase images. Imaging regions of high susceptibility result in phase shifts greater than ±π, characterized by black and white banding or aliasing in the phase image. This artifact is commonly seen above the paranasal sinuses and the ear canals. Adding a 3D Laplacian unwrapping pre-processing step before the conventional SWI reconstruction effectively removes the aliasing and reveals the smoother underlying phase change.

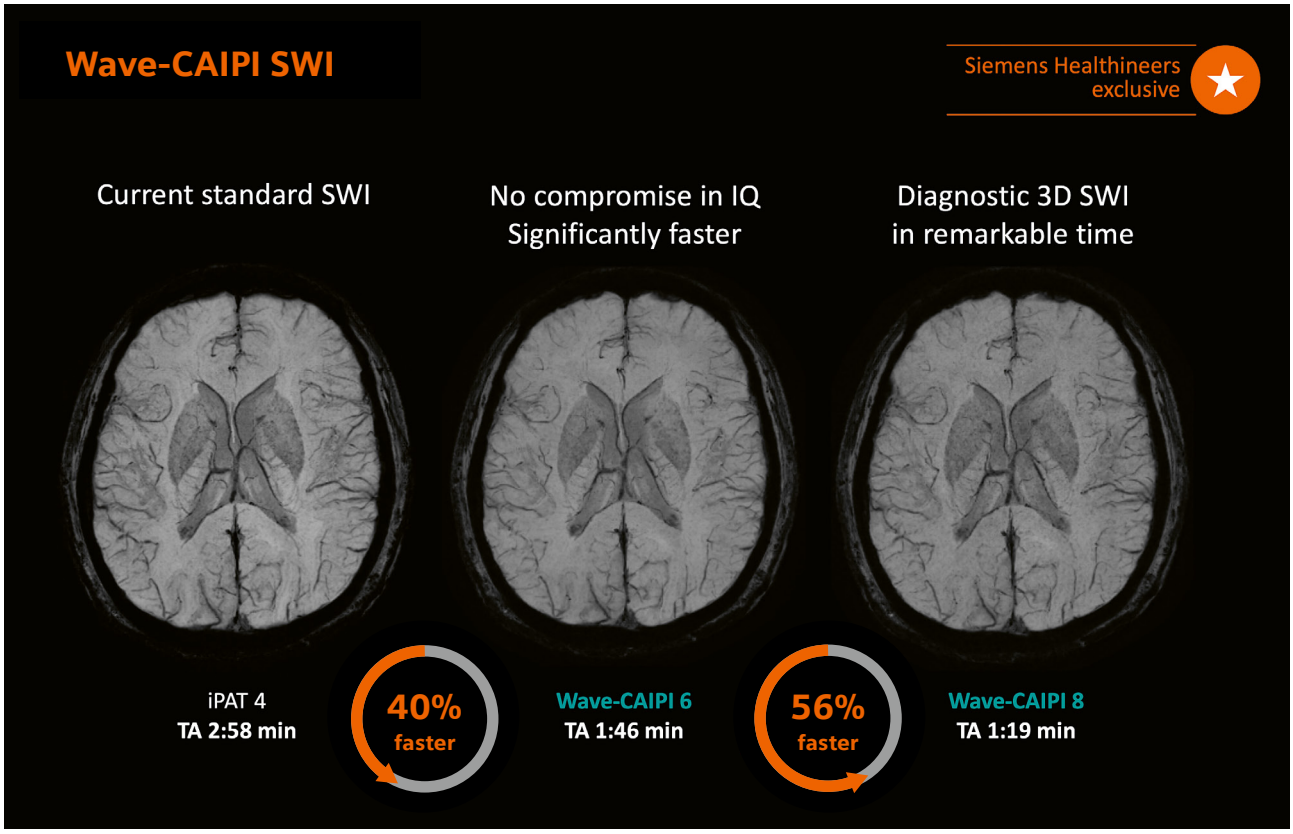

1 Comparison of product SWI and Wave-CAIPI SWI acquired on a 3T MAGNETOM Vida with a voxel size of 0.6 × 0.6 × 2.0 mm^3. This novel SWI technique, unique to Siemens Healthineers, can significantly accelerate diagnostic 3D-SWI and enables imaging twice as fast as standard SWI.

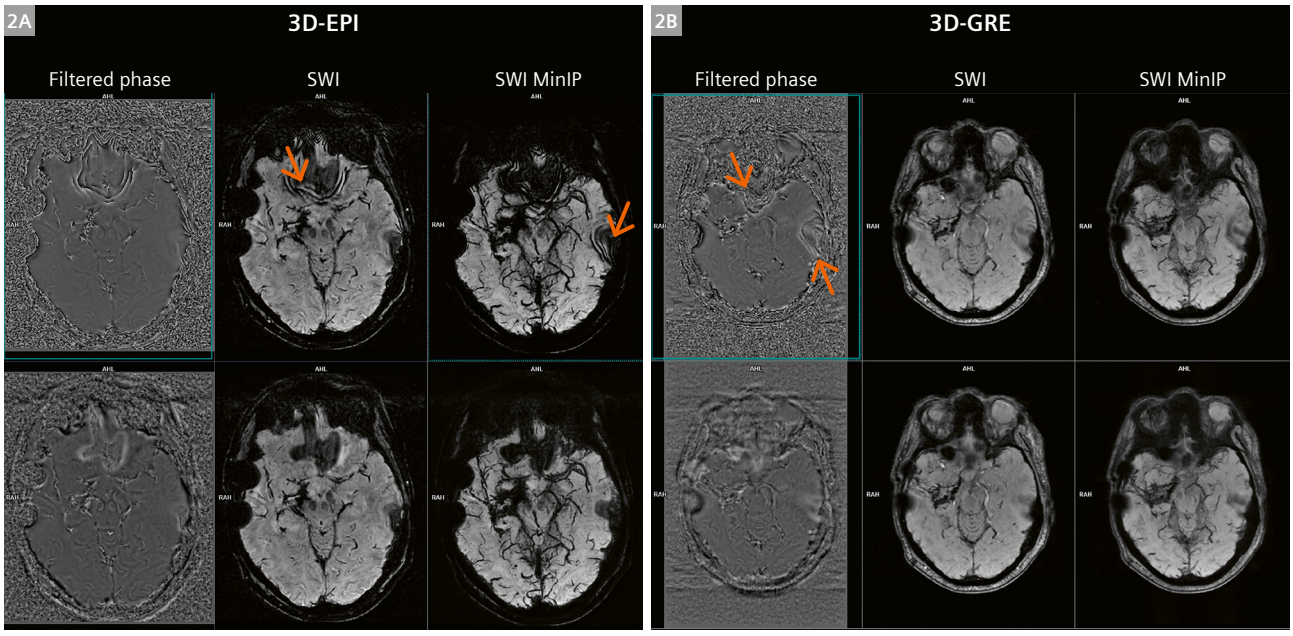

2 Effect of improved phase processing for susceptibility-weighted imaging (SWI): filtered phase (left), SWI image (middle) and minimum intensity projection MinIP (right). Artifacts are visible in regions with large off-resonances above the paranasal sinuses in the frontal lobe and ear canals (top row), causing sudden phase changes or aliasing (phase wraps). They are visibly improved using phase unwrapping (bottom row). The SWI images are from an MS patient scanned with 3D-EPI at an echo time of 40 ms **(2A)** and multi-echo 3D-GRE (ten TEs from 5 to 44 ms) **(2B)**.
Data courtesy of Dr. Sylvie Grand and Professor Alexandre Krainik (CHU Grenoble), and Marylene Delcey (Siemens Healthineers, France).

Imaging parameters:

3D-EPI: FOV 169 x 200 mm^2, 72 slices, resolution 0.39 × 0.39 × 1.5 mm^3 (interpolated), TE 40 ms, TR 80 ms, FA 20°, BW 369 Hz/px, no PAT, EF 11, TA 1:43 min.

3D-GRE: FOV 176 × 256 mm^2, 120 slices, resolution 0.41 × 0.39 × 1.0 mm^3 (interpolated), 10 TEs 5.3–44 ms, $TE_{average}$ 25 ms, TR 50 ms, FA 15°, BW 407 Hz/px, PAT 3, TA 5:25 min.

Consequently, the resultant SWI images show improved signal recovery with minimal artifacts in these areas of high susceptibility.

The impact of enhanced phase processing on SWI is illustrated in Figure 2. This MS patient was scanned using a product 3D-EPI at an echo time of 40 ms (Fig. 2A) and a product multi-echo 3D-GRE (ten echo times ranging from 5 to 44 ms) (Fig. 2B). In the first row, the filtered phase (left), SWI image (middle), and minimum intensity projection (MinIP) (right) depicts phase aliasing artifacts in regions with significant off-resonances (see arrows in the frontal lobe and ear canals). These artifacts result from the sudden phase wraps, which are difficult to resolve with conventional SWI processing. In the bottom row, the same images are presented after employing the Laplacian phase unwrapping pre-processing step. This process visibly improves the artifacts seen in the top row.

To further demonstrate the ability of the multi-echo 3D-GRE acquisition to enhance the signal-to-noise ratio compared to utilizing just a single echo, we present images from another MS patient. (Fig. 3A) SWI images (top panel) and SWI MinIP images (bottom) were captured using a multi-echo 3D-GRE acquisition with ten echoes ranging from 5 to 44 ms. Five out of the ten echo times are displayed, along with the combined images with an average echo time of 25 ms. A comparison is made with a single-echo acquisition on the left (Fig. 3B), highlighting the visibly improved signal- and contrast-to-noise observed in the combined images from the ten echoes. Various weightings for the echo combination can be chosen, such as equal weighting, echo-time-dependent weighting, or user-defined custom weighting.

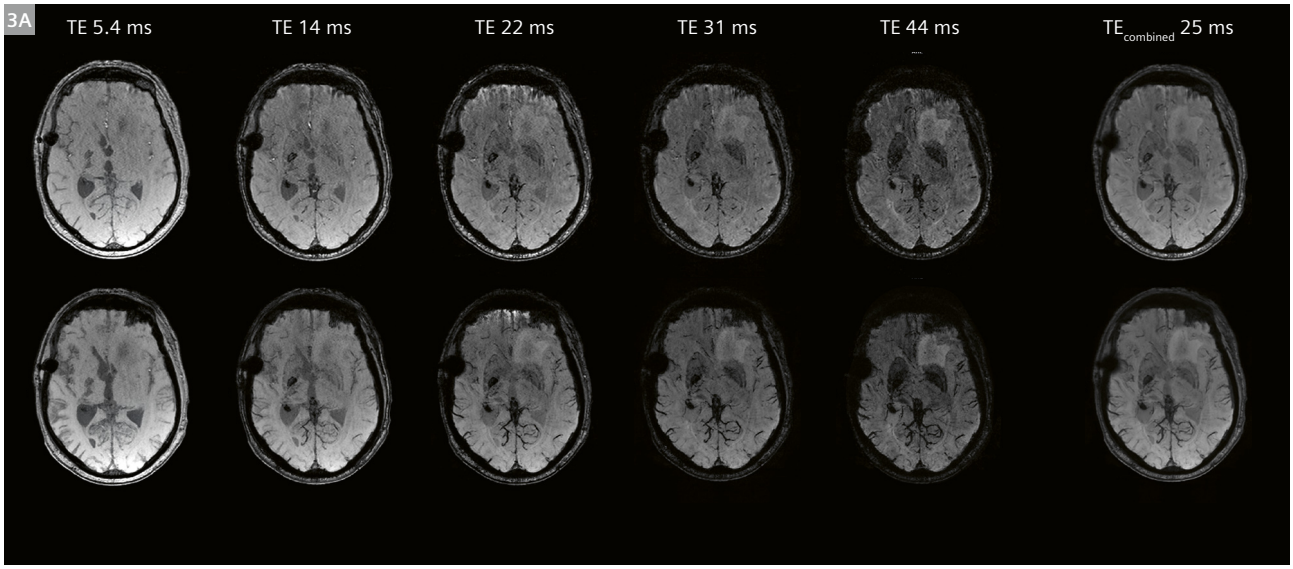

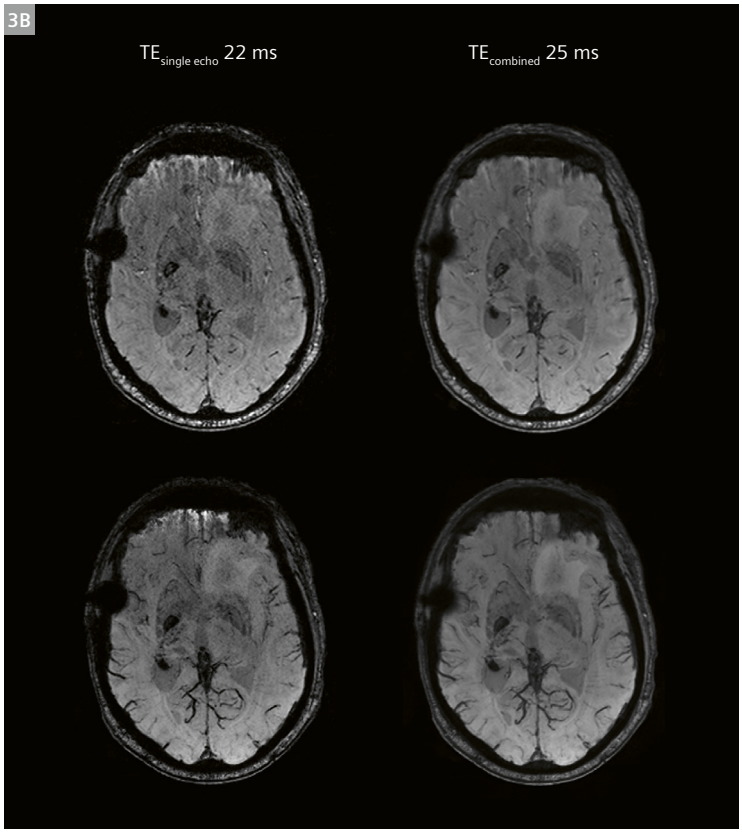

3 Signal-to-noise improvements for SWI using multi-echo 3D-GRE. **(3A)** SWI (top) and SWI MinIP (bottom) from an MS patient with a multi-echo 3D-GRE acquisition using ten echo times from 5 to 44 ms. Five images out of the ten echo times are shown, as well as the combined images with average TE 25 ms. **(3B**) Compared to a single-echo acquisition (left), the combined images from ten echoes show visibly improved signal- and contrast-to-noise.

Imaging parameters: Same 3D-GRE patient data as in Figure (2B) with a different slice shown.

Quantitative Susceptibility Mapping (QSM)

An overview of data acquisition and processing for SWI and QSM is shown in Figure 4. For QSM, the key steps include phase unwrapping, creating a mask from the magnitude image, and applying the background field correction and dipole inversion. In contrast, SWI involves filtering the signal phase, weighting it by the magnitude, and performing a MinIP across slices (Fig. 4A). In the SWI MinIP, the effects of susceptibility from the venous blood make it well-suited to visualizing veins in the brain. However, the processing steps required for SWI imaging make the data incompatible with the steps required to compute QSM. To overcome this, the research implementation reconstructs SWI and QSM in parallel pipelines.

This package now enables the inline post-processing of phase data to generate QSM data using two methods: **Total Generalized Variation (TGV)** [29–31] and **Morphology Enabled Dipole Inversion (MEDI)** [32]. For each method, either a morphological (for brain only) or phase-fidelity-based masking procedure like in ROMEO [31] is required to identify the region of interest for further processing. The package supports three different post processing methods:

- The **MEDI QSM algorithm** applies a choice of background field correction algorithms including the Projection onto Dipole Fields (PDF) and Laplacian Boundary Value (LBV) methods.
- The **TGV QSM algorithm** combines the Laplacian phase unwrapping, background phase removal, and dipole inversion into a single optimization problem. The TGV algorithm is implemented in the Compute Unified Device Architecture (CUDA, NVIDIA, Santa Clara, CA, USA) on the graphics processing unit (GPU) and can be configured by the number of iterations and the regularization parameters. GPU processing time for a 1 mm isotropic whole-brain data set is 5–10 seconds.
- In addition, the **two-step TGV QSM algorithm** [30] is a recent extension of the TGV method which performs two successive TGV reconstructions. The first reconstruction is processed with a mask that only contains reliable susceptibility sources. The second reconstruction applies an additional mask that includes both reliable and less-reliable sources. The different phase-based masks are determined using different thresholds applied to the phase-fidelity image – a normalized phase quality metric. The two-step TGV algorithm aims to be more robust to less-reliable or high-susceptibility sources, which often introduce streaking into the QSM image. The two successive reconstructions are subsequently combined to provide one resultant QSM image.

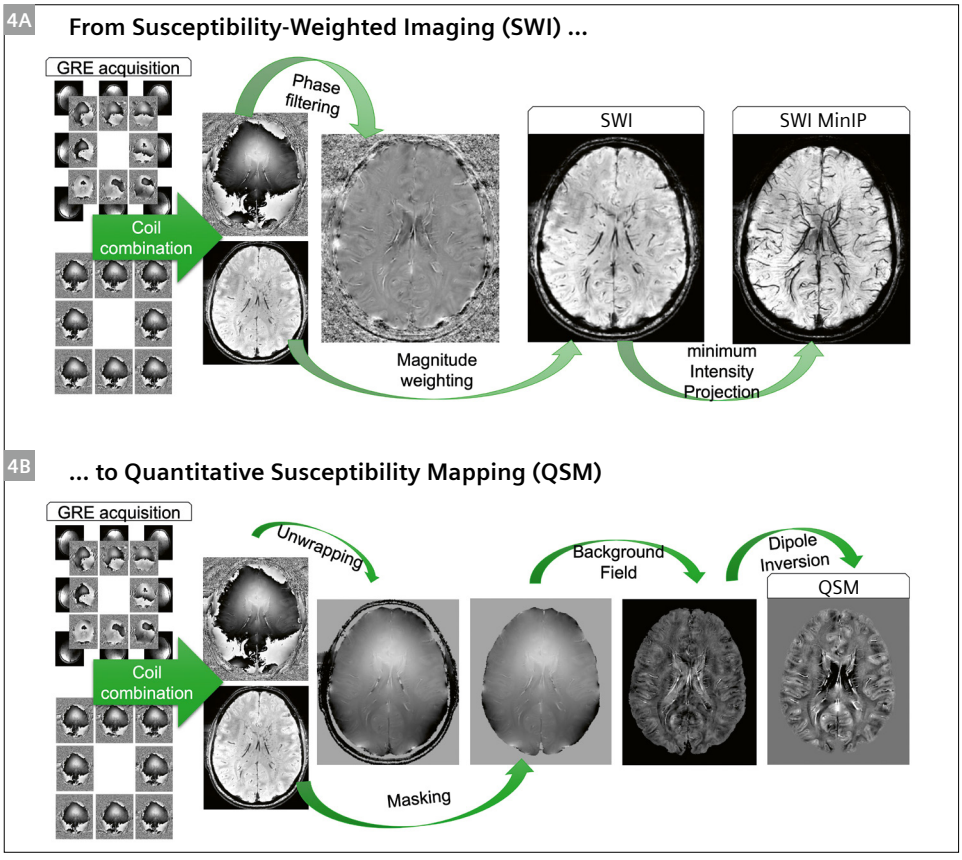

4 Overview of data acquisition and processing for SWI and QSM. **(4A)** SWI is computed from GRE data by filtering the signal phase, weighting it by the magnitude and then minimum intensity projection (MinIP) across slices. In the SWI MinIP, the susceptibility effects from the venous blood make it perfectly suited to visualizing veins in the brain. **(4B)** The steps that are typically required to compute QSM are phase unwrapping, calculating a brain mask, background field removal, and dipole inversion.

In Figure 5, three slices are presented, each processed with different QSM algorithms, along with a derived Susceptibility Map-Weighted Imaging (SMWI) contrast (see below). The QSM maps are scaled to the range of [-100, 300] ppb, which is equivalent to [-0.1, 0.3] ppm. In Figure 5A, the two-step TGV algorithm is featured. The processing mask is created from a phase fidelity map and is thereby independent from brain anatomy. In Figure 5B, the MEDI algorithm is employed, utilizing brain masking with slight erosion of image edges to mitigate artifacts in the dipole inversion process. The overall representation of deep brain structures is well-preserved in both QSM modalities, with MEDI showing a tendency for increased QSM values compared to TGV, while TGV images appear less regularized (smoothed) in comparison to MEDI.

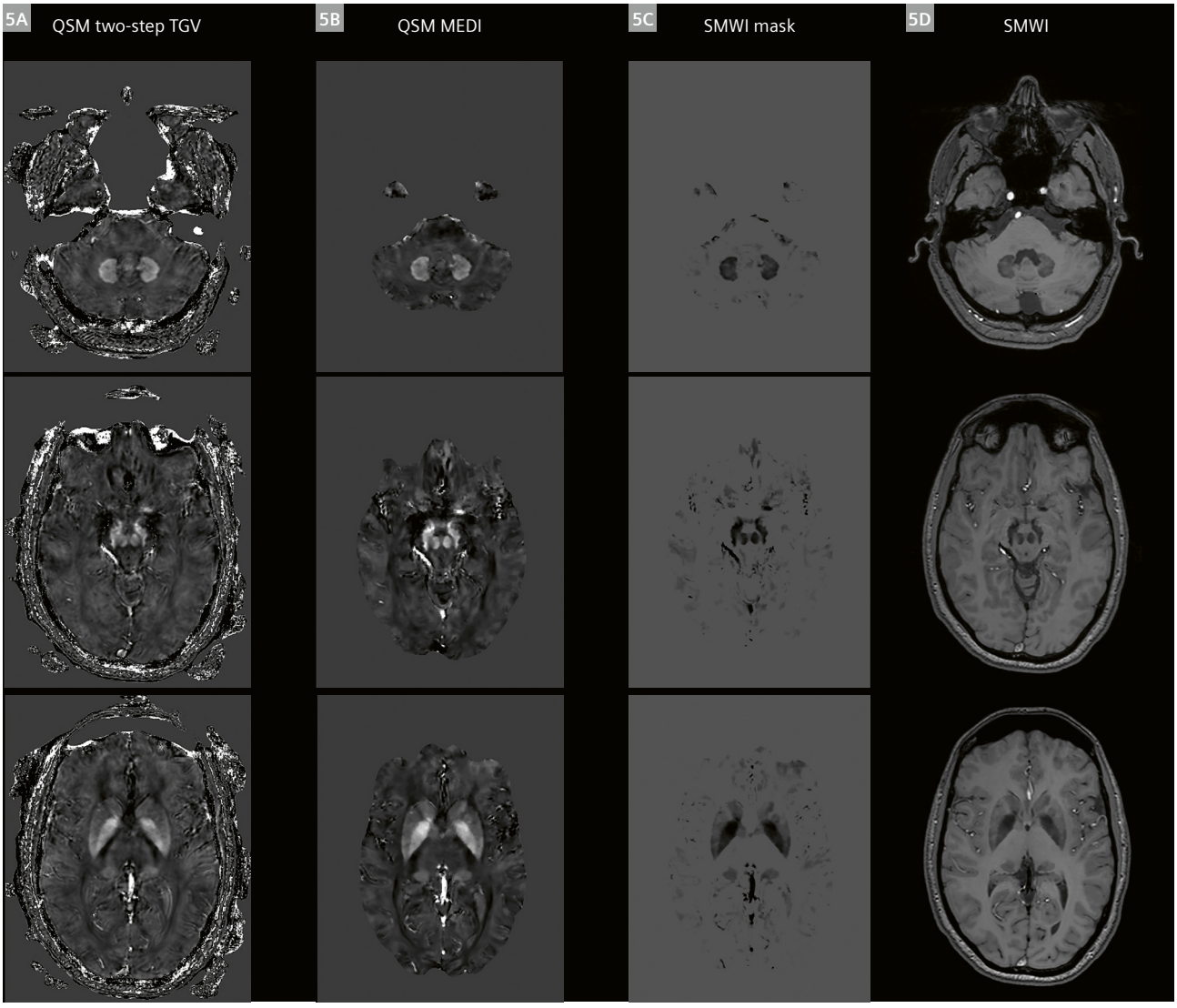

5 Three slices processed with different QSM algorithms and the derived SMWI contrast. The QSM maps are scaled to [-100, 300] ppb, equivalent to [-0.1, 0.3] ppm. **(5A)** The two-step TGV algorithm creates the processing mask from a phase fidelity map and is thus independent from brain anatomy. **(5B)** The MEDI algorithm uses brain masking, and the image edges are somewhat eroded to avoid artifacts in the dipole inversion process. Overall, deep brain structures are represented well in both QSM modalities. MEDI has a tendency for increased QSM values compared to TGV, while the TGV images appear less regularized (smoothed) compared to MEDI. **(5C)** SMWI mask with a weighting factor between [0, 1] calculated from Figure 5B, QSM MEDI images. **(5D)** SMWI images derived from the SMWI mask and the underlying magnitude image.

Imaging parameters:

3D-GRE: FOV 178 × 256 mm^2, 128 slices, resolution 0.5 × 0.5 × 1.0 mm^3 (interpolated), 6 s TE 5.4–27 ms, $TE_{average}$ 16 ms, TR 31 ms, FA 20°, BW 407 Hz/px, PAT 2, Deep Resolve Boost and Sharp, TA 4:25 min.

Susceptibility Map-Weighted Imaging (SMWI)

SMWI has recently been proposed to enhance the contrast-to-noise ratio for visualizing structures containing iron. Recent studies, such as the one conducted by Sung and colleagues in 2022, have demonstrated that SMWI surpasses SWI in assessing nigral hyperintensity at 3T [33].

SMWI images are generated from the QSM image, following the method outlined by Sung-Min Gho et al. in 2014 [34]. This involves combining the magnitude image with a QSM-based weighting factor, introducing an alternative yet analogous contrast to SWI.

The paramagnetic susceptibility mask (with positive susceptibility values, $th_{value} > 0$) is designed as follows [34]:

$$S_{mask}(x) = \begin{cases} 0 & th_{value} < S_{value}(x) \\ (th_{value} - S_{value}(x)) / th_{value} & 0 < S_{value}(x) \leq th_{value} \\ 1 & otherwise \end{cases}$$

By default, SMWI employs a paramagnetic susceptibility mask (pSMWI) with a preset threshold of 1 ppm (1000 ppb) and a multiplication factor denoted as m = 4. In the context of different pathologies, the utilization of a diamagnetic susceptibility mask (dSMWI) with negative susceptibility values is considered advantageous, although it is not explicitly illustrated in the present context.

The pSMWI mask is shown in Figure 5C and is characterized by a weighting factor within the range [0, 1], and is computed from the QSM MEDI images illustrated in Figure 5B. The SMWI images in Figure 5D are subsequently generated by combining the SMWI mask with the underlying magnitude image.

3D deep learning *k*-space-to-image reconstruction

The standard image reconstruction of the 3D-GRE and 3D-EPI sequences include GRAPPA and CAIPIRINHA. The research 3D-EPI application herein allows for flexible EPI train lengths, segmentation, and acceleration factors [35, 36]. Both sequences also include the 3D deep learning *k*-space-to-image reconstruction method Deep Resolve Boost, and the super-resolution method Deep Resolve Sharp.

The deep learning reconstruction comprises two independent, sequential processing steps. Firstly, Deep Resolve Boost images are generated on the acquired resolution using a variational network architecture with six iterations that alternate between parallel imaging reconstruction and 3D image regularizations using U-nets. The network parameters were determined through supervised training based on several hundreds of fully sampled 3D datasets of healthy volunteers from various body regions. Secondly, for Deep Resolve Sharp, the obtained images were interpolated using a deep learning-based super-resolution algorithm, with a factor-of-two interpolation. Both steps were implemented in PyTorch trained on a dedicated GPU cluster and with networks exported for prospective use in the scanner reconstruction pipeline.

Figure 6 displays QSM maps scaled within the [-100, 300] ppb range, obtained from the two sequences 3D-GRE and 3D-EPI, employing different image reconstructions. The QSM algorithm applied in this context was TGV.

The 3D-EPI protocol parameters were matched to those of the five-echo 3D-GRE, with an echo time set to 20 ms. The five-echo 3D-GRE had echo times ranging from 6.6 to 34 ms, with an average echo time of 20 ms. The acquisition time (TA) for the 3D-GRE sequence was 5:35 min. To align with the five echoes of the 3D-GRE, the EPI factor for 3D-EPI was set to five, rendering this sequence approximately four times faster (TA 1:41 min). The minimum repetition time (TR) was selected, specifically TR 39 ms for 3D-GRE, and TR 56 ms for 3D-EPI, respectively.

The signal- and contrast-to-noise ratio in the QSM maps exhibits a slight decrease when comparing 3D-GRE to the faster 3D-EPI acquisitions, as depicted in Figure 6A from left to right. This reduction aligns with our anticipated outcome from signal-to-noise calculations. However, when the data is reconstructed using the 3D deep learning *k*-space-to-image reconstruction method (Deep Resolve Boost), the QSM image quality and structural features are comparable to standard reconstruction. This holds true even with the approximate four-fold increase in speed, as illustrated in Figure 6B from left to right.

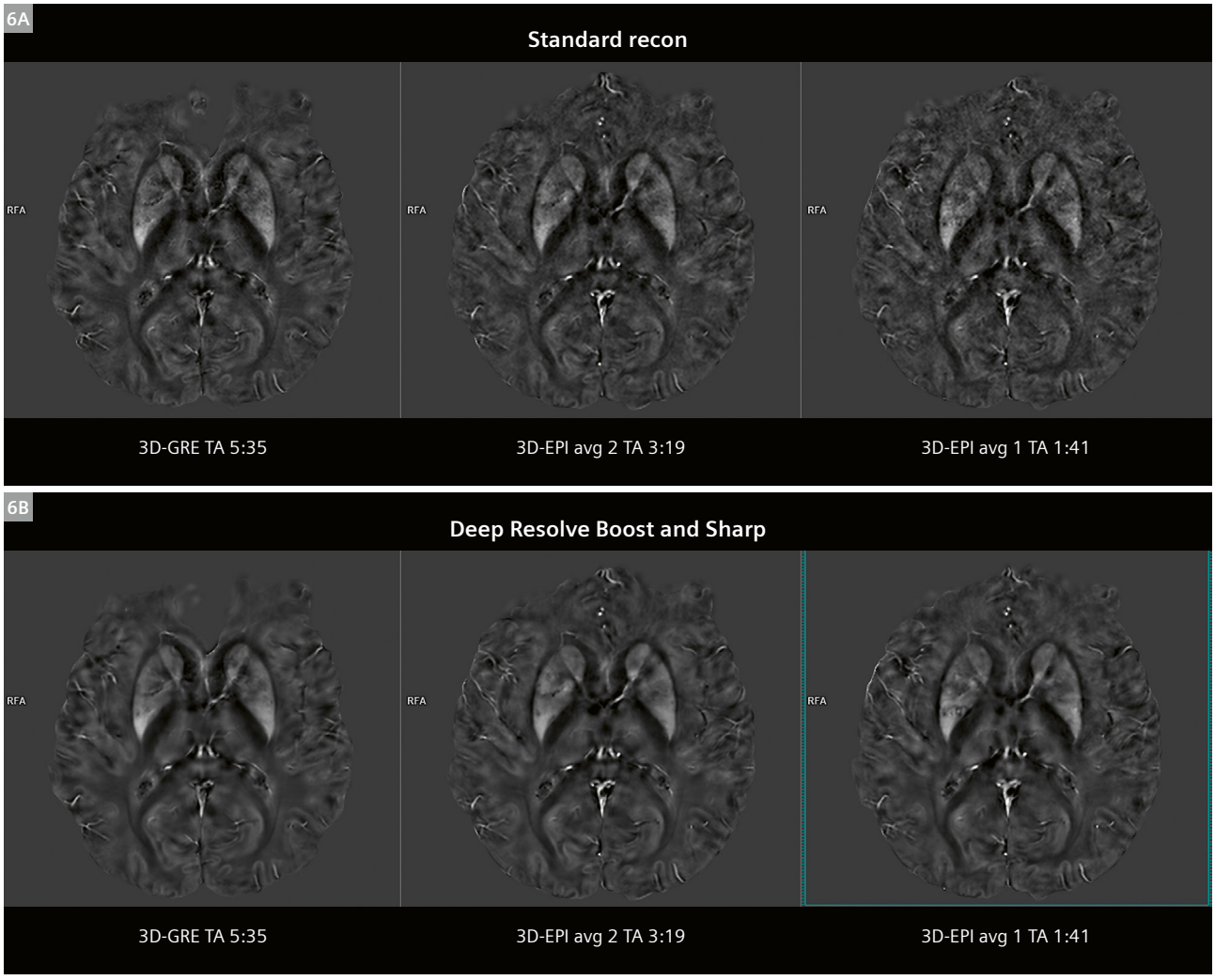

6 QSM maps scaled to [-100, 300] ppb from different sequences, 3D-GRE and 3D-EPI, and different image reconstructions. **(6A)** 3D-EPI used matched parameters with an echo time of 20 ms compared to 3D-GRE. The EPI factor of five in 3D-EPI compared to five echoes with 3D-GRE makes this sequence approx. four times faster. The QSM contrast-to-noise ratio decreases with the faster acquisition (left to right). **(6B)** Using the 3D deep learning *k*-space-to-image reconstruction (Deep Resolve Boost) could mostly preserve the QSM image quality even with an approx. 4-time increase in speed.

Imaging parameters: FOV 224 × 224 mm², 64 slices, resolution 0.35 × 0.35 × 2.0 mm³ (interpolated), PAT 3, standard reconstruction vs. Deep Resolve Boost and Sharp, TGV algorithm.
3D-GRE: 5 TEs 6.6 – 34 ms, $TE_{average}$ 20 ms, TR 39 ms, FA 15°, BW 200 Hz/px, TA 5:35 min.
3D-EPI: TE 20 ms, TR 56 ms, FA 21°, BW 284 Hz/px, EF 5, TA 3:19 / 1:41 min with avg 2 / 1.

Nigrosome 1 ("swallow tail") imaging in substantia nigra

Publications hint that SWI at 3T or 7T could potentially function as a novel imaging biomarker for idiopathic Parkinson's disease (IPD) [33] by improving the ability to observe the nigral hyperintensity or nigrosome 1. Recent studies [33] also propose that the novel SMWI methods may further enhance the ability to observe changes to nigrosome 1. These studies also provide evidence that the robust diagnostic performance of the novel SMWI methods remains consistent in a multicenter setting with various MRI scanners, indicating the potential applicability of SMWI in assessing nigrostriatal degeneration in individuals with parkinsonism.

Figure 7 displays QSM and SMWI images of a healthy subject, with slices planned along the AC–PC line. The nigrosome 1 "swallow tail" in the substantia nigra is clearly highlighted in both QSM and SMWI images (Fig. 7A). The SMWI image is presented in 3D orthogonal planes of nigrosome 1 (Fig. 7B).

Notably, using a 64-channel head-neck coil, the 0.65 mm isotropic dataset with whole-brain coverage was acquired in a total time of 3:12 min. This efficiency is achieved through (1) effective sampling with 3D-EPI and (2) employing 3D deep learning *k*-space-to-image reconstruction (Deep Resolve Boost).

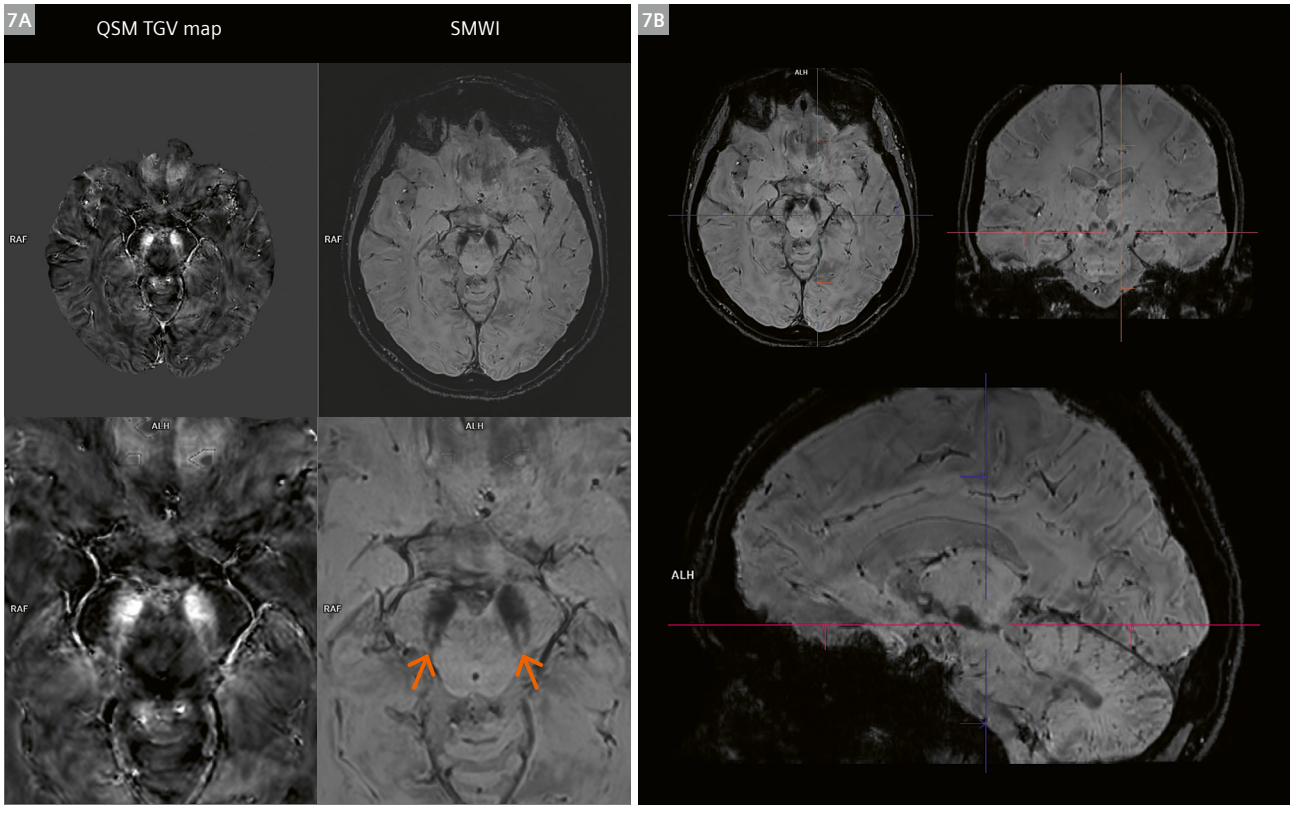

7 QSM and SMWI of a healthy subject with slices planned along the AC–PC line. **(7A)** The nigrosome 1 "swallow tail" in the substantia nigra is nicely contrasted in both QSM and SMWI images. **(7B)** SMWI image in 3D orthogonal planes of nigrosome 1. Remarkably, the 0.65 mm^3 isotropic dataset with whole-brain coverage could be acquired in 3:12 min using a 64-channel head-neck coil. This is made possible by using (1) efficient sampling with 3D-EPI and (2) 3D deep learning *k*-space-to-image reconstruction (Deep Resolve Boost).

Imaging parameters:

3D-EPI: FOV 250 × 250 mm^2, 196 slices, resolution 0.33 × 0.33 × 0.65 mm^3 (interpolated), TE 27 ms, TR 51 ms, FA 15°, BW_{RO} 651 Hz/px, BW_{PE} 30 Hz/px (46 Hz/mm), EF 19, slcOS 14%, slcPF 6/8, PAT 2, Deep Resolve Boost and Sharp, avg 2, TA 3:12 min.

Conclusions

In conclusion, this article showcases significant advancements in Susceptibility-Weighted Imaging (SWI) and Quantitative Susceptibility Mapping (QSM) techniques, offering notable improvements in image quality and diagnostic potential. Through utilization of 3D Laplacian phase unwrapping, SWI processing demonstrates enhanced signal recovery and reduced artifacts in areas of high susceptibility. The implementation of multi-echo 3D-GRE techniques further enhances signal-to-noise ratio in SWI images.

The introduction of QSM and SMWI emerges as a promising approach to achieve superior diagnostic performance compared to SWI alone. The synergy of efficient sampling techniques such as 3D-EPI and 3D deep learning *k*-space-to-image reconstruction (Deep Resolve Boost) can significantly accelerate the image acquisition while preserving image quality for these novel clinical imaging techniques.

These advancements contribute to the evolving landscape of neuroimaging, paving the way for enhanced diagnostic accuracy and efficiency in evaluating neurodegenerative disorders. The search for and validation of clinically valuable biomarkers, such as the improved visualization of nigrosome 1 and the "swallow tail" sign for idiopathic Parkinson's disease, are now more accessible through this research.

Acknowledgments

The collaborative development of the QSM and 3D-EPI research package involved Professor Markus Barth and his team at the Center for Advanced Imaging, The University of Queensland, Australia, which includes Monique Tourell and Saskia Bollmann.

Jinsuh Kim from Emory University School of Medicine, Atlanta, USA (present address), played a pivotal role in developing the TGV GPU code in collaboration with Christian Langkammer and Kristian Bredies from the University of Graz, Austria.

The ROMEO code was developed through a collaboration with Professor Simon Robinson from the High Field MR Center, Medical University of Vienna, Austria, and Barbara Dymerska from the Wellcome Centre for Human Neuroimaging, University College London, UK.

Professors Pascal Spincemaille and Yi Wang from the Cornell MRI Research Lab, NY, USA, provided the QSM MEDI code.

Dr. Sylvie Grand and Professor Alexandre Krainik from CHU Grenoble, France, and Marylene Delcey, Siemens Healthineers, France, contributed the patient SWI data presented in Figure 2. Protocol optimization and subject data for Figure 7 were provided by Melanie Adam, master's student at Siemens Healthineers, Erlangen, Germany.

The authors express their gratitude to Professor Jongho Lee from the Department of Electrical and Computer Engineering, and to Professor Eung Yeop Kim from Radiology at Samsung Medical Center, Seoul, Korea, for their insightful discussions about Susceptibility Map-Weighted Imaging.

References

1 Reichenbach JR, Haacke EM. High-resolution BOLD venographic imaging: a window into brain function. NMR Biomed. 2001;14(7–8):453–67.
2 Haacke EM, Mittal S, Wu Z, Neelavalli J, Cheng YC. Susceptibility-weighted imaging: technical aspects and clinical applications, part 1. AJNR Am J Neuroradiol. 2009;30(1):19–30.
3 Mittal S, Wu Z, Neelavalli J, Haacke EM. Susceptibility-weighted imaging: technical aspects and clinical applications, part 2. AJNR Am J Neuroradiol. 2009;30(2):232–52.
4 Wang Y, Spincemaille P, Liu Z, Dimov A, Deh K, Li J, et al. Clinical quantitative susceptibility mapping (QSM): Biometal imaging and its emerging roles in patient care. J Magn Reson Imaging. 2017;46(4):951–971.
5 Eckstein K, Bachrata B, Hangel G, Widhalm G, Enzinger C, Barth M, et al. Improved susceptibility weighted imaging at ultra-high field using bipolar multi-echo acquisition and optimized image processing: CLEAR-SWI. Neuroimage. 2021;237:118175.
6 Cummings J, Rabinovici GD, Atri A, Aisen P, Apostolova LG, Hendrix S, et al. Aducanumab: Appropriate Use Recommendations Update. J Prev Alzheimers Dis. 2022;9(2):221–230.
7 Duyn J. MR susceptibility imaging. J Magn Reson. 2013;229:198–207.
8 Haacke EM, Liu S, Buch S, Zheng W, Wu D, Ye Y. Quantitative susceptibility mapping: current status and future directions. Magn Reson Imaging. 2015;33(1):1–25.
9 Wang Y, Liu T. Quantitative susceptibility mapping (QSM): Decoding MRI data for a tissue magnetic biomarker. Magn Reson Med. 2015;73(1):82–101.
10 Chen W, Gauthier SA, Gupta A, Comunale J, Liu T, Wang S, et al. Quantitative susceptibility mapping of multiple sclerosis lesions at various ages. Radiology. 2014;271(1):183–92.
11 Langkammer C, Liu T, Khalil M, Enzinger C, Jehna M, Fuchs S, et al. Quantitative susceptibility mapping in multiple sclerosis. Radiology. 2013;267(2):551–9.
12 Li X, Harrison DM, Liu H, Jones CK, Oh J, Calabresi PA, et al. Magnetic susceptibility contrast variations in multiple sclerosis lesions. J Magn Reson Imaging. 2016 Feb;43(2):463–73.
13 Rahmanzadeh R, Galbusera R, Lu PJ, Bahn E, Weigel M, Barakovic M, et al. A New Advanced MRI Biomarker for Remyelinated Lesions in Multiple Sclerosis. Ann Neurol. 2022;92(3):486–502.
14 Schweser F, Deistung A, Lehr BW, Reichenbach JR. Differentiation between diamagnetic and paramagnetic cerebral lesions based on magnetic susceptibility mapping. Med Phys. 2010;37(10):5165–78.
15 Straub S, Laun FB, Emmerich J, Jobke B, Hauswald H, Katayama S, et al. Potential of quantitative susceptibility mapping for detection of prostatic calcifications. J Magn Reson Imaging. 2017;45(3):889–898.
16 Alkemade A, de Hollander G, Keuken MC, Schäfer A, Ott DVM, Schwarz J, et al. Comparison of T2*-weighted and QSM contrasts in Parkinson's disease to visualize the STN with MRI. PLoS One. 2017;12(4):e0176130.
17 Devos D, Moreau C, Devedjian JC, Kluza J, Petrault M, Laloux C, et al. Targeting chelatable iron as a therapeutic modality in Parkinson's disease. Antioxid Redox Signal. 2014;21(2):195–210.

18 Bilgic B, Pfefferbaum A, Rohlfing T, Sullivan EV, Adalsteinsson E. MRI estimates of brain iron concentration in normal aging using quantitative susceptibility mapping. Neuroimage. 2012;59(3):2625–35.
19 Acosta-Cabronero J, Williams GB, Cardenas-Blanco A, Arnold RJ, Lupson V, Nestor PJ. In vivo quantitative susceptibility mapping (QSM) in Alzheimer's disease. PLoS One. 2013;8(11):e81093.
20 Moon Y, Han SH, Moon WJ. Patterns of Brain Iron Accumulation in Vascular Dementia and Alzheimer's Dementia Using Quantitative Susceptibility Mapping Imaging. J Alzheimers Dis. 2016;51(3):737–45.
21 Hwang EJ, Kim HG, Kim D, Rhee HY, Ryu CW, Liu T, et al. Texture analyses of quantitative susceptibility maps to differentiate Alzheimer's disease from cognitive normal and mild cognitive impairment. Med Phys. 2016;43(8):4718.
22 van Bergen JM, Hua J, Unschuld PG, Lim IA, Jones CK, Margolis RL, et al. Quantitative Susceptibility Mapping Suggests Altered Brain Iron in Premanifest Huntington Disease. AJNR Am J Neuroradiol. 2016;37(5):789–96.
23 Deistung A, Stefanescu MR, Ernst TM, Schlamann M, Ladd ME, Reichenbach JR, et al. Structural and Functional Magnetic Resonance Imaging of the Cerebellum: Considerations for Assessing Cerebellar Ataxias. Cerebellum. 2016;15(1):21–25.
24 Schweitzer AD, Liu T, Gupta A, Zheng K, Seedial S, Shtilbans A, et al. Quantitative susceptibility mapping of the motor cortex in amyotrophic lateral sclerosis and primary lateral sclerosis. AJR Am J Roentgenol. 2015;204(5):1086–92.
25 Sharma SD, Fischer R, Schoennagel BP, Nielsen P, Kooijman H, Yamamura J, et al. MRI-based quantitative susceptibility mapping (QSM) and R2* mapping of liver iron overload: Comparison with SQUID-based biomagnetic liver susceptometry. Magn Reson Med. 2017;78(1):264–270.
26 He Q, Liu Z, Wang Y, Du J. Ultrashort Echo Time Quantitative Susceptibility Mapping (UTE-QSM) of Cortical Bone. Proceedings of the 23rd Annual Meeting ISMRM Toronto, ON, Canada. 2015. Vol. 1725.
27 Polak D, Cauley S, Bilgic B, Wald L, Setsompop K. Ultrafast Multi-contrast High-resolution 3D Brain MRI: a Technical Description of Wave-CAIPI. MAGNETOM Flash.2020;76(1):17–20.
28 Filho ALG, Conklin J, Rapalino O, Schaefer P, Huang S. Ultrafast Multi-Contrast High-Resolution 3D Brain MRI: Clinical Evaluation of Wave-CAIPI Acceleration in SWI, MPRAGE, FLAIR, SPACE. ↗ MAGNETOM Flash.2020;76(1):21–27.
29 Langkammer C, Bredies K, Poser BA, Barth M, Reishofer G, Fan AP, et al. Fast quantitative susceptibility mapping using 3D EPI and total generalized variation. Neuroimage. 2015;111:622–30.
30 Stewart AW, Robinson SD, O'Brien K, Jin J, Widhalm G, Hangel G, et al. QSMxT: Robust masking and artifact reduction for quantitative susceptibility mapping. Magn Reson Med. 2022;87(3):1289–1300.
31 Dymerska B, Eckstein K, Bachrata B, Siow B, Trattnig S, Shmueli K, et al. Phase unwrapping with a rapid opensource minimum spanning tree algorithm (ROMEO). Magn Reson Med. 2021;85(4):2294–2308.
32 Liu J, Liu T, de Rochefort L, Ledoux J, Khalidov I, Chen W, et al. Morphology enabled dipole inversion for quantitative susceptibility mapping using structural consistency between the magnitude image and the susceptibility map. Neuroimage. 2012;59(3):2560–8.
33 Sung YH, Kim JS, Yoo SW, Shin NY, Nam Y, Ahn TB, et al. A prospective multi-centre study of susceptibility map-weighted MRI for the diagnosis of neurodegenerative parkinsonism. Eur Radiol. 2022;32(5):3597–3608.
34 Gho SM, Liu C, Li W, Jang U, Kim EY, Hwang D, et al. Susceptibility map-weighted imaging (SMWI) for neuroimaging. Magn Reson Med. 2014;72(2):337–46.
35 Jin J, Tourell M, Sati P, Liu K, Derbyshire J, O'Brien K, et al. Segmented 3D EPI with CAIPIRINHA for Fast, High-Resolution T2*-weighted Imaging. Proceedings of the Annual Meeting ISMRM 2021.
36 Jin J, Nickel D, Pfeuffer J, Tourell M, Stewart A, Bollmann S. Fast, High-resolution Whole Brain SWI and QSM with CAIPIRINHA 3D-EPI and Deep Learning Reconstruction. Proceedings of the Annual Meeting ISMRM 2024.

Contact

Dr. Josef Pfeuffer
Siemens Healthineers AG
SHS DI MR RCT CLS NEUR
Erlangen
Germany
josef.pfeuffer@siemens-healthineers.com


Josef Pfeuffer


Steffen Bollmann


Korbinian Eckstein


Ashley Wilton Stewart